INSTITUT DE FRANCE
Académie des sciences

Comptes Rendus

Mécanique

Mohammad Hadi Namdar Ghalati and Hamed Ghafarirad

Continuous deformation analysis and contact force estimation for pneumatic bending actuators interacting with environment

Volume 351 (2023), p. 43-58

https://doi.org/10.5802/crmeca.167

e-ISSN : 1873-7234

Comptes Rendus
Mécanique
2023, Vol. 351, p. 43-58
`https://doi.org/10.5802/crmeca.167`

Short paper / *Note*

Continuous deformation analysis and contact force estimation for pneumatic bending actuators interacting with environment

Mohammad Hadi Namdar Ghalati [a] **and Hamed Ghafarirad** *, [a]

[a] Department of Mechanical Engineering, Amirkabir University of Technology,
Tehran, Iran
E-mails: hadi.namdar@gmail.com (M. H. Namdar Ghalati), ghafarirad@aut.ac.ir
(H. Ghafarirad)

Abstract. Soft bending actuators show high adaptability for applications such as rehabilitation or grasping. Although constant curvature assumption has been extensively used for free motion modeling, these actuators do not bend circularly when interacting with the environment. In such situation, conventional bending sensors cannot provide useful information on their shape. In this paper, the Finite Rigid Elements approach is utilized to model the behavior of a soft pneumatic bending actuator in free motion and contact. With this method, the variable curvature configuration under different external loads can be modeled. Then, the contact force between the actuator and an object located in a specific position is estimated utilizing the Gradient Descent optimization method. Experimental results verified the combinatorial proposed approach for both force estimation and structure deformation.

Keywords. Soft bending actuator, Static modeling, Deformation analysis, Force estimation, Finite rigid elements method.

Manuscript received 3 June 2022, revised 12 November 2022 and 18 December 2022, accepted 20 December 2022.

1. Introduction

Unlike past decades when the soft robotics area was just a topic in laboratories, in recent years, it has found its way into industries and has become a significant interdisciplinary branch of science. It involves many fields of engineering such as mechanical, electrical, chemical, etc. The unique features of soft robots, including compliance, safety, adaptability, and more similarities to nature [1], make these types of robots attractive to researchers [2]. However, these particular attributes bring more complexity, and in comparison with conventional rigid robots, modeling and control of the soft robots are much more complicated and case-dependent.

---

[*] Corresponding author.

The concept of soft robotics encompasses a wide range of robots with flexible bodies actuated by tendons [3, 4], fluids [5], dielectric elastomers [6], smart materials [7], etc. Among different types of soft robots, soft actuators with pneumatic actuation have the ability to exert considerable force while being safe enough. For this reason, they are utilized in various applications, including manipulators [8, 9], grippers [10, 11], rehabilitation robots [12], bio-inspired robots [13], etc. Generally, soft pneumatic bending actuators are divided into two categories, i.e. multi-chamber (PneuNets) [14] and fiber-reinforced actuators [15]. Although both types are functional and can generate bending deformation, the structure of the latter type provides the feasibility to produce compound deformations e.g. twisting and elongation added to the bending [16, 17].

However, the nonlinear behavior of the material utilized in these actuators makes the process of modeling complicated. Polygerinos *et al.* derived a static model for a fiber-reinforced bending actuator by neglecting the effect of external constraints and using the Neo Hookean theory for hyperelastic material [18]. Wang *et al.* investigated the behavior of the actuator by resorting to the Lagrange method in free motion as well [19]. Finite-Element Method (FEM) is a suitable approach to deal with the complexity of analytical methods for nonlinear materials. In this regard, Gharavi *et al.* analyzed the behavior of a soft bending actuator using FEM [20].

Despite the fact that the study of free motion behavior brings valuable perspective, there are usually positional constraints caused by the environment in real applications such as grasping or rehabilitation. In these cases, the actuator interacts with other objects, and the interaction force would be a significant term. Several approaches have been proposed to consider the effect of external forces. In this regard, assuming the actuator as a beam with a large deflection [21] is a method that has been widely used. Zhou *et al.* considered a cantilever beam with an intrinsic curvature that is under the effect of a couple of concentrated fixed forces. They calculated the effect of external loads on the beam profile using the Euler–Bernoulli beam theory [22]. Namdar *et al.* developed the previous method and investigated the configuration of a soft fiber-reinforced bending actuator under the effect of different types of concentrated forces and inlet pressure [23]. However, none of the above-mentioned research takes the contact situation and positional constraints into account. In addition, one of the most applied approaches in the field of soft actuators' modeling is the Cosserat rod theory [24]. Despite the accuracy and generality of this method, its high computational cost and complexity limit its application in real-time cases such as control systems.

Besides the mentioned challenges in the modeling of soft bending actuators in contact, the lack of position and force sensing systems is still a significant hinder to taking advantage of soft actuators. A flex sensor, which is a variable resistor, has been widely used by many researchers to measure and control the bending angle of the actuator [25, 26]. But in spite of being soft, this sensor could not measure a non-constant curvature. To overcome this issue, Davarzani *et al.* designed a sensor system with four inertial measurement unit (IMU) sensors to obtain the kinematics of their finger-like soft actuator [27]. The developed system can determine the curvature of the actuator but significantly reduces its softness. Lu *et al.* designed and fabricated a soft sensing system using liquid conductive metal, which can measure the pressure and strain [28]. However, this system cannot determine the non-constant deformation of the actuator. Godage *et al.* utilized a fiber optic shape sensor (FOSS) to achieve the curvature of the actuator [29]. Despite the softness and high-frequency response, the proposed sensory system has a high-cost implementation and can only measure the curvature of the actuator, and does not provide any data about external forces. In regards to external force measurement, most of the research works used load cell, which is not an appropriate choice in applications such as soft gloves and soft grippers [30–32]. The soft array sensory system devised by Navarro *et al.* is more efficient to detect the contact position and estimate the contact force [33].

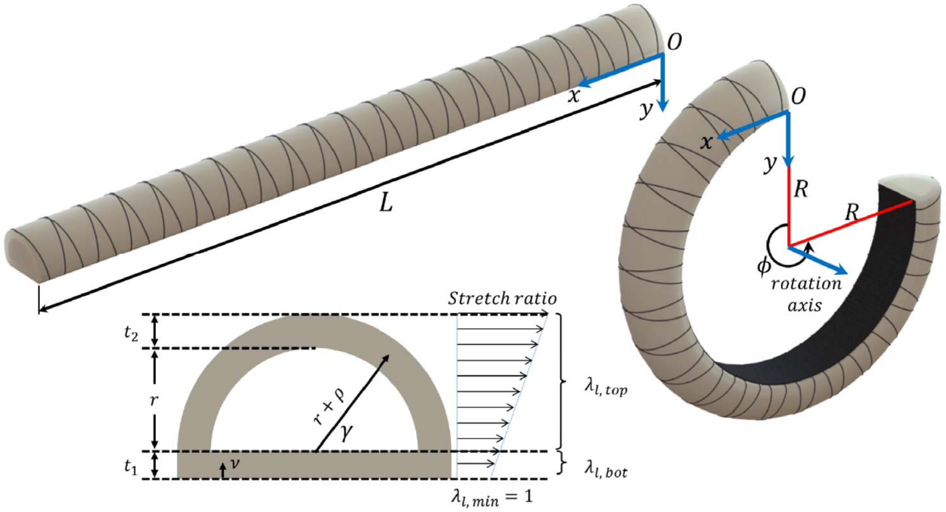

Figure 1. Actuator element schematic.

Concerning the mentioned challenge, this research proposes the Nonlinear Finite Rigid Elements (NFRE) methods to cover both the material nonlinearity and actuator behavior in free motion and contact. By resorting to this method, both non-constant continuous deformation and contact forces can be determined simultaneously. For this purpose, first, the material nonlinear behavior is modeled by the energy approach. Then, the NFRE method is utilized to express the static behavior in free motion and interacting with the environment. This way, the non-constant deformation of the soft actuator can be determined. Based on the proposed approach, the Gradient Descent optimization method is used to estimate the contact force between the soft bending actuator and an obstacle located in a specific location. These methods are validated using empirical tests.

2. Actuator structure and its behavior analysis

The main concept behind the soft bending actuators is the difference between the neutral axis and the position of the actuation force, which causes a moment that bends the actuator. In this research, we will use a soft pneumatic reinforced bending actuator in order to validate the theoretical method; however, the method can be utilized for other types of bending actuators. In this actuator, a semi-cylindrical chamber which is made of a hyperelastic material constructs the main part. The chamber deforms in all directions, i.e., longitudinal, radial, and circumferential, effortlessly while inflating. The radial deformation of the chamber is prevented by wrapping two helical reinforcing fibers around it symmetrically. In addition, the neutral axis of the chamber is displaced by attaching a fabric layer to its flat side. Figure 1 shows the actuator's components and its configuration in inflated and unpressurized conditions.

In Figure 1, L, r, t_1, and t_2 are geometrical parameters used to represent the length, the inner radius, the flat part thickness, and the cylindrical thickness of the actuator, respectively. ν, ρ, and γ are auxiliary coordinates that are used to denote any point on the cross-section of the actuator. In addition, λ_l is the longitudinal stretch ratio. The value of λ_l is one on the constraint layer—denoted by $\lambda_{l,\min}$—and increases as it takes distance from the constraint layer. For simplicity purposes, $\lambda_{l,\text{bot}}$ and $\lambda_{l,\text{top}}$ are used to show the stretch ratio in the flat and cylindrical parts.

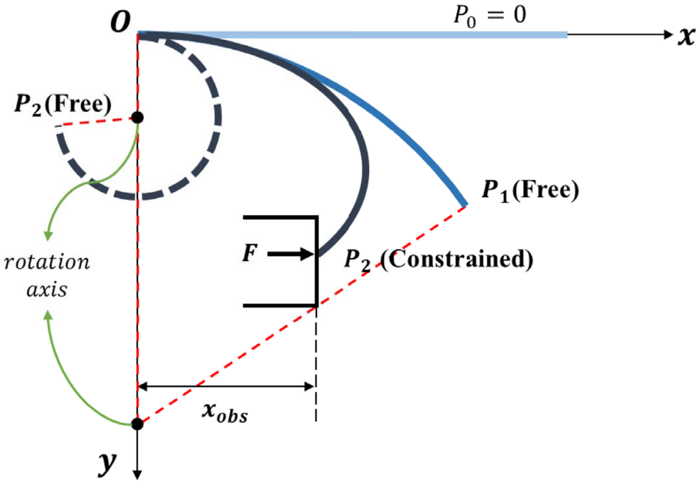

Figure 2. Schematic of the actuator in free and constrained conditions. The actuator has a constant curvature in free motion, while its profile is not circular in the constrained situation. P denotes the internal pressure, and F is the external force.

In this research, it is assumed that the stretch ratio increases linearly. Finally, R and ϕ are the actuator's curvature radius and angle, respectively.

Due to the homogeneity of the actuator structure, it bends with a constant curvature as long as there are no external loads and constraints. However, as soon as it reaches an obstacle, the interaction force between the actuator and the environment disrupts the constant curvature behavior, and the actuator curvature will not remain constant. Figure 2 depicts the actuator behavior in free and constrained conditions.

3. Energy-based modeling of the soft actuator in free motion

In the pneumatic soft bending actuators, the pressurized air is the actuation factor. Also, research has shown that the constant curvature assumption is valid for the bending actuators with a uniform structure when there is no applied external effect ($L = R\phi$ with L the length of the actuator, R its bending curvature which is constant when no external load is applied, and ϕ its total bending angle). Therefore, the actuator curvature could be defined as a function of inlet pressure. However, when the actuator is affected by an external load such as gravity or an obstacle, its curvature would not remain constant. In this case, the soft actuator is a system with infinite degrees of freedom. Before studying the actuator in the constraint condition, its behavior in free motion will be reviewed based on the energy approach.

3.1. *Generalized force*

While the actuator is inflated, the generalized force due to the increase of the inlet pressure can be determined using Equation (1).

$$F_G = P\frac{\partial V_c}{\partial \phi} \tag{1}$$

where F_G, P, V_c, and ϕ are generalized force, inlet pressure, chamber volume, and bending angle, respectively. The volume of the chamber can be calculated by the difference between the total (V_T) and elastomer (V_e) volumes, see Equation (2)

$$V_c = V_T - V_e. \tag{2}$$

According to the incompressible assumption, the elastomer has a constant volume in any condition. Therefore,

$$\frac{\partial V_c}{\partial \phi} = \frac{\partial}{\partial \phi}(V_T - V_e) = \frac{\partial V_T}{\partial \phi}. \tag{3}$$

In addition, based on the constant curvature assumption, by inflating the actuator in the absence of external effects, the actuator has a constant curvature. Besides, the reinforcement fibers and fabric layer force the cross-section of the actuator to remain unchanged under different pressure. So, by using Pappus's theorem, the total volume can be determined. To do so, the cross-section is divided into two parts, i.e., top and bottom.

$$\begin{cases} A_{\text{top}} = \dfrac{\pi}{2}(r+t_2)^2 \\ \overline{d}_{\text{top}} = \dfrac{L}{\phi} + t_1 + \dfrac{4}{3\pi}(r+t_2) \end{cases} \tag{4}$$

$$\begin{cases} A_{\text{bot}} = 2t_1(r+t_2) \\ \overline{d}_{\text{bot}} = \dfrac{L}{\phi} + \dfrac{t_1}{2} \end{cases} \tag{5}$$

where A_{top} and A_{bot} are the areas of the top and bottom sections, and d_{top} and d_{bot} the distances between the center of these areas and the rotation axis along the y-axis shown in Figure 1. All other parameters are illustrated in Figure 1 and defined in the paragraph below that. Consequently, the total volume can be calculated using Equation (6).

$$V_T = \phi \sum A_i \overline{d}_i = \left[\frac{2}{3}(r+t_2)^3 + \frac{\pi t_1}{2}(r+t_2)^2 + t_1^2(r+t_2)\right]\phi + \left[\frac{\pi L}{2}(r+t_2)^2 + 2Lt_1(r+t_2)\right]. \tag{6}$$

Finally,

$$F_G = \left[\frac{2}{3}(r+t_2)^3 + \frac{\pi t_1}{2}(r+t_2)^2 + t_1^2(r+t_2)\right]P = C_P P. \tag{7}$$

3.2. *Potential energy*

If the actuator deforms in the horizontal plane, the only potential energy stored in the actuator is strain energy. Based on the Neo-Hookean model for incompressible hyperelastic material, the strain energy of the elastomer can be obtained using Equation (8)

$$E_s = \int_{V_e} \frac{\mu}{2}(I_1 - 3)\,\mathrm{d}V \tag{8}$$

where μ is the shear modulus which depends on the material, $I_1 = \sum_{i=1}^{3} \lambda_i^2$ is the first invariant of stretch tensor, and λ_i-s are the principal stretch ratios. By assuming the actuator as a thin-walled tube λ_1, λ_2, and, λ_3 are longitudinal (λ_l), circumferential (λ_c), and radial (λ_r), respectively. Reinforcement fibers around the actuator resist the variation of the actuator radius which means that $\lambda_c = 1$. Using the incompressible material assumption ($\prod_{i=1}^{3} \lambda_i = 1$), we can write that $\lambda_r = 1/\lambda_l$. The stretch ratio on the fabric layer is one, since it is an inextensible material. A function whose value is one on the fabric layer and increases linearly by distancing from the layer is a decent approximation for the longitudinal stretch ratio function. For simplicity, the stretch ratio function is defined as a piecewise function Equation (9) with two sub-functions for the top and bottom parts, i.e., semi-cylindrical and rectangular sections.

$$\begin{cases} \lambda_{l,\text{top}} = 1 + \dfrac{(t_1 + (r+\rho)\sin\gamma)\phi}{L}, & \rho \in [0, t_2] \\ \lambda_{l,\text{bot}} = 1 + \dfrac{\nu\phi}{L}, & \nu \in [0, t_1]. \end{cases} \tag{9}$$

Therefore,

$$E_{s,\mathrm{top}} = \mu L \int_0^{t_2} \int_0^{\pi/2} \left[\left(1 + \frac{(t_1 + (r+\rho)\sin\gamma)\phi}{L}\right)^2 + \left(1 + \frac{(t_1 + (r+\rho)\sin\gamma)\phi}{L}\right)^{-2} - 2 \right] (r+\rho)\,\mathrm{d}\gamma\,\mathrm{d}\rho \tag{10}$$

$$E_{s,\mathrm{bot}} = \mu L(r + t_2) \int_0^{t_1} \left[\left(1 + \frac{v\phi}{L}\right)^2 + \left(1 + \frac{v\phi}{L}\right)^{-2} - 2 \right] \mathrm{d}v. \tag{11}$$

Equations (10) and (11) can be simplified by the use of the following expansion.

$$(1+z)^{-2} = 1 - 2z + 3z^2 - 4z^3 + \cdots. \tag{12}$$

Consequently,

$$E_s = E_{s,\mathrm{top}} + E_{s,\mathrm{bot}} = c_1\phi^2 + c_2\phi^3 \tag{13}$$

$$c_1 = \frac{4\mu t_1^3 (r + t_2)}{3L} + \frac{4\mu}{L} \int_0^{t_2} \int_0^{\pi/2} (t_1 + (r+\rho)\sin\gamma)^2 (r+\rho)\,\mathrm{d}\gamma\,\mathrm{d}\rho \tag{14}$$

$$c_2 = -\frac{\mu t_1^4 (r + t_2)}{L^2} - \frac{4\mu}{L^2} \int_0^{t_2} \int_0^{\pi/2} (t_1 + (r+\rho)\sin\gamma)^3 (r+\rho)\,\mathrm{d}\gamma\,\mathrm{d}\rho. \tag{15}$$

3.3. *Equilibrium equation*

According to the principle of virtual work, which relates the potential energy (U) to the generalized force F_G that produces a curvature ϕ, a static model is obtained as Equation (16), knowing that the only potential energy stored in the actuator is the strain energy ($U = E_s$).

$$\delta U = F_G \delta\phi \rightarrow a\phi + b\phi^2 = P \tag{16}$$

where $a = 2c_1/C_P$ and $b = 3c_2/C_P$ with C_P defined in Equation (7).

As stated before, the constant curvature assumption is valid until the actuator bends in the absence of any external constraint. Consequently, the derived equation, i.e., Equation (16), is deficient in constraint situations. Therefore, to model the effect of external loads on the actuator curvature, an approach based on the Nonlinear Finite Rigid Elements method will be presented in the next section.

4. Nonlinear finite rigid elements method for free motion and contact

Finite Rigid Elements Method is usually utilized to model the continuum structures [34]. By discretizing the actuator into a series of n links with nonlinear torsional springs in the joints, and using the Denavit–Hartenberg method, a model for the elements' position could be derived in the static situation. Figure 3 shows the schematic of the actuator as well as the defined parameters and coordinates.

It should be noted that the nth coordinate is located at the tip point and is parallel to the $(n-1)$th coordinate. In order to derive the static model for the actuator, the Denavit–Hartenberg parameters for the consecutive coordinates are defined in Table 1.

Table 1. DH parameters for the actuator

i	a_{i-1}	α_{i-1}	θ_i	d_i
1	dl	0	θ_1	0
2	dl	0	θ_2	0
$\vdots$	dl	0	θ_i	0
$n-1$	dl	0	θ_{n-1}	0
$n \geq 2$	dl	0	0	0

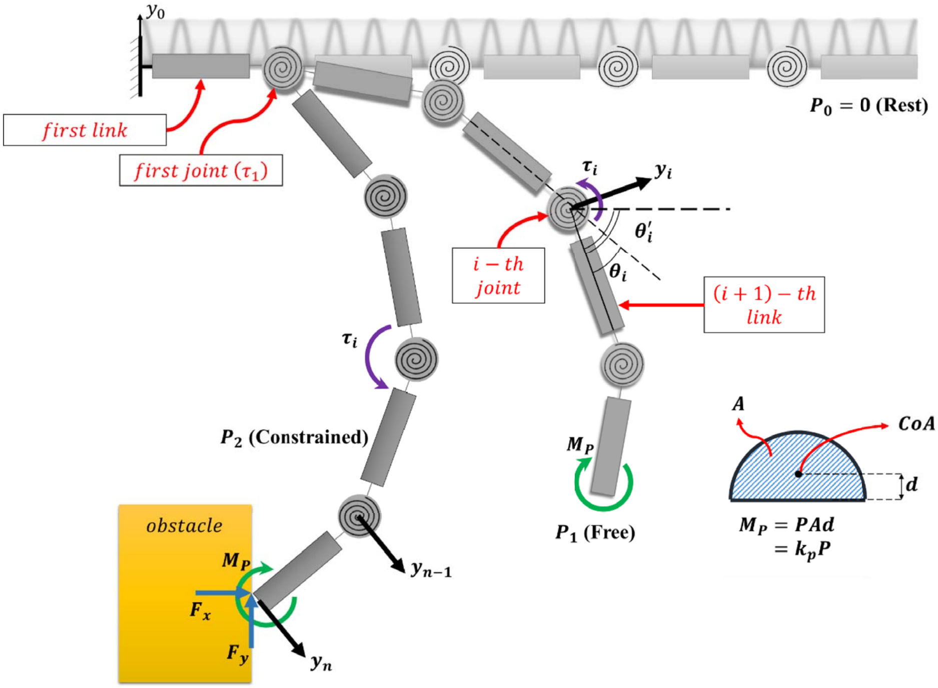

Figure 3. Schematic of the actuator under the effect of internal pressure, modeled as a moment (M_P), and concentrated forces F_x and F_y at the tip.

Where dl is the elements' length, and $\theta_i - s$ are the relative angle of the consecutive coordinates, shown in Figure 3. According to the DH parameters, the matrix that transforms each coordinate axis to the inertia coordinate (${}^0T_i$) could be determined using Equation (17),

$$ {}^0T_i = \begin{bmatrix} c\theta'_i & -s\theta'_i & 0 & dl\sum_{t=0}^{i-1} c\theta'_t \\ s\theta'_i & c\theta'_i & 0 & dl\sum_{t=0}^{i-1} s\theta'_t \\ 0 & 0 & 1 & 0 \\ 0 & 0 & 0 & 1 \end{bmatrix}, \quad i = 1,2,\dots,n,\ \theta'_0 = \theta_0 = 0 \tag{17} $$

where $c\theta = \cos\theta$ and $s\theta = \sin\theta$. In addition, θ'_i is the absolute angle of each coordinate ($\theta'_i = \sum_{j=0}^{i}\theta_j$.) Therefore, the Jacobian matrix, defined in the base coordinate, (${}^0J_i$) can be calculated as well.

$$ {}^0J_i = dl \begin{bmatrix} -\sum_{t=i}^{n-1} s\theta'_t \\ \sum_{t=i}^{n-1} c\theta'_t \\ 0 \end{bmatrix}, \quad i = 1,2,\dots,n-1. \tag{18} $$

It should be mentioned that the Jacobian matrix includes both position and orientation terms in general. However, for a planar serial robot with revolute joints, the last row of the Jacobian matrix would be a vector of ones. Therefore, the orientation section of the Jacobian could be omitted, and the related terms added separately (see Equation (20)).

While the actuator is inflated, the inlet pressure could be considered as an equivalent force applied to the end wall of the actuator at its center of area (CoA), shown in Figure 3. Due to the difference of the neutral axis and CoA position, the force acts as a moment at the end tip of the actuator as expressed in Equation (19).

$$M_p = k_P P \tag{19}$$

M_p is the moment created at the tip of the actuator due to the inlet pressure, and k_p is a constant value that converts inlet pressure to the moment. Moreover, the effect of the contact between the actuator and the obstacle could be modeled as a couple of horizontal and vertical fixed direction forces (F_x, F_y) at the end tip. This means that the interactive force between the actuator and the environment has a constant direction and does not depend on the orientation of the actuator.

The moment and forces that are exerted on the actuator make the torsional springs in the joints twist and create reaction torque. Equation (20) determines the torque (τ) created in each joint as the effect of inlet pressure as well as external contact, and Equation (21) calculates the reaction torque of springs in that joint.

$$\tau_i = {}^0J_i^T F + M_p \tag{20}$$

$$\tau_i = k_1\theta_i + k_2\theta_i^2. \tag{21}$$

As was mentioned below the Equation (18), in this method, the orientation section of the Jacobian matrix, which is a vector of ones, is omitted, and the effect of the moment (M_p) has been added separately in Equation (20).

In Equation (21), k_1 and k_2 are the coefficients of the nonlinear spring that is used to model our actuator, with the hypothesis that its nonlinear behavior can be represented as a second order polynomial. This nonlinearity is caused by the instinct nonlinear behavior of the utilized material, i.e., silicon rubber. Indeed, the energy-based modeling, presented in Section 3, experimental data, and the model described in [23] validate this assumption. However, this nonlinearity depends on many parameters such as material shore, the ratio of hardener, the curing procedure, etc. Although in special cases, a specific actuator may show lower nonlinearity, a 2nd order polynomial is a more general function that covers most designs.

Finally, using Equations (18) to (21) the configuration of the actuator in contact with an obstacle can be derived as expressed in Equation (22).

$$k_1\theta_i + k_2\theta_i^2 + F_x dl \sum_{t=i}^{n-1} s\theta'_t - F_y dl \sum_{t=i}^{n-1} c\theta'_t = k_P P \quad i = 1,2,\ldots,n-1. \tag{22}$$

According to Equation (22), in the absence of the obstacle $(F_x = F_y = 0)$, the relation between the inlet pressure and the joints' angle is a second-order polynomial function. In addition, due to the constant curvature assumption, θ_i-s are equal, and $\theta'_n = \phi$. Consequently,

$$k_1\left(\frac{\phi}{n-1}\right) + k_2\left(\frac{\phi}{n-1}\right)^2 = k_P P. \tag{23}$$

The values $k_1/(n-1)k_P = a$ and $k_2/(n-1)^2 k_P = b$ show the resistance of the actuator against deformation, and obviously should not depend on the number of elements. Therefore, a torsional spring with constant coefficients K_1 and K_2 is defined as the equivalent elasticity of the springs system, these coefficients being defined as a function of the elements' number and equivalent elasticity as expressed in Equation (24).

$$\begin{cases} k_1 = K_1(n-1) \\ k_2 = K_2(n-1)^2. \end{cases} \tag{24}$$

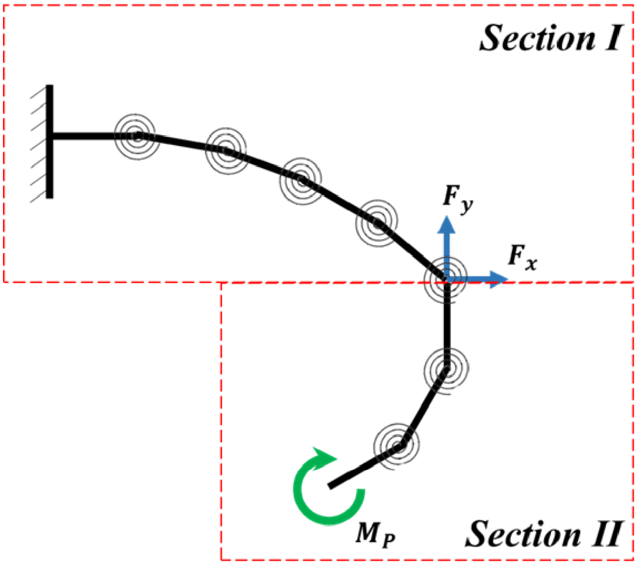

Figure 4. Schematic of the actuator under the effect of internal pressure, modeled as a moment (M_P), and concentrated forces F_x and F_y exerted along the actuator.

According to Equation (17), the tip position can be determined using Equation (25).

$$\begin{cases} x_{\text{tip}} = \sum\limits_{t=0}^{n-1} dl c\theta'_t \\ y_{\text{tip}} = \sum\limits_{t=0}^{n-1} dl s\theta'_t . \end{cases} \tag{25}$$

Remark. The contact between the actuator and the environment may happen not only at the end-tip but also at another point on the actuator, as shown in Figure 4. In this condition, the actuator can be divided into two parts: The first part is an actuator with a force at its end-tip, and the second part is an actuator which is pressurized in the absence of the external constraints and attached to the first part. Making the assumption that a fixed force is exerted on a point located somewhere other than at the end-tip of the actuator, e.g., on the jth joint, the following couple of equations can be utilized to model the situation.

$$\begin{cases} k_1\theta_i + k_2\theta_i^2 + F_x dl \sum\limits_{t=i}^{j-1} s\theta'_t - F_y dl \sum\limits_{t=i}^{j-1} c\theta'_t = k_P P & i = 1, 2, \ldots, j-1 \\ k_1\theta_i + k_2\theta_i^2 = k_P P & i = j,\ j+1, \ldots, n-1. \end{cases} \tag{26}$$

5. Force estimation and configuration detection for position constraints

So far, a static model is derived for the actuator, i.e., the actuator's configuration can be obtained in the presence of the inlet pressure and external forces. However, in some applications the obstacle position (x_{obs}) is determined and the actuator should exert the desired force on the object, e.g. soft grippers. In these cases, to estimate the force exerted by the pressurized actuator on the obstacle, the inverse model has to be solved. The following method can estimate the force (F) that an actuator with a certain inlet pressure (P) exerts on a vertical frictionless wall located in a specific horizontal position. In addition, the frictionless assumption does not limit

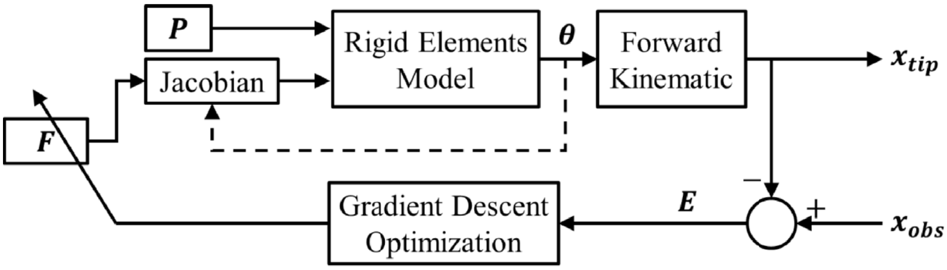

Figure 5. Force estimation method diagram.

the generality of the method since, in applications where the vertical force is nonzero, its value is known or can be calculated easily. For instance, while the actuator is utilized in a gripper, the vertical force is the object's weight.

Figure 5 depicts the block diagram of the inverse static model. In this approach, for a given input pressure, the value of the external force should be explored in which the position of the end tip (x_{tip}) coincides with the obstacle position (x_{obs}). The exploration would be accomplished by an optimization algorithm.

By defining the cost function as Equation (27) and the error as Equation (28), the algorithm was designed to minimize the cost function.

$$W = \tfrac{1}{2}E^2 \tag{27}$$

$$E = x_{\text{tip}} - x_{\text{obs}}. \tag{28}$$

According to the gradient descent method, the force can be determined iteratively using Equation (29).

$$\Delta F_x = -\eta \frac{\partial W}{\partial F_x} = -\eta \frac{\partial W}{\partial E}\frac{\partial E}{\partial F_x} = -\eta E \frac{\partial E}{\partial F_x}, \quad \eta > 0 \tag{29}$$

where

$$\frac{\partial E}{\partial F_x} = \frac{\partial x_{\text{tip}}}{\partial F_x} = \frac{\partial}{\partial F_x}\left[\sum_{t=0}^{n-1} dl c\theta'_t\right] = -dl \sum_{t=0}^{n-1} \frac{\partial \theta'_t}{\partial F_x} s\theta'_t. \tag{30}$$

Therefore,

$$\Delta F_x = -\eta E \frac{\partial E}{\partial F_x} = \eta dl E \sum_{t=0}^{n-1} \frac{\partial \theta'_t}{\partial F_x} s\theta'_t. \tag{31}$$

As a result, the applied force can be determined as follows:

$$F'_x = F_x + \eta dl \left(\sum_{t=0}^{n-1} dl c\theta'_t - x_{\text{obs}}\right) \sum_{t=0}^{n-1} \frac{\partial \theta'_t}{\partial F_x} s\theta'_t. \tag{32}$$

6. Experimental results

In order to examine the validity of the theoretical model, an experimental setup consisting of a soft bending actuator and all necessary sensors was developed. The setup consists of pneumatic items, including a 16-bars air compressor and a Festo 5/3-way proportional solenoid valve to inflate the soft actuator. In addition, three sensors, including a Festo digital pressure sensor (SDE1) with 0.01-bar accuracy, an Intel RealSense-SR300 digital camera, and a load cell, were utilized to measure the actuator inlet pressure, its curvature, and external force, respectively. Finally, a computer receives sensors' data and sends commands to the solenoid valve using a NI data acquisition card (PCI-6052E). Figure 6 shows the different parts of the experimental setup and the signal flow.

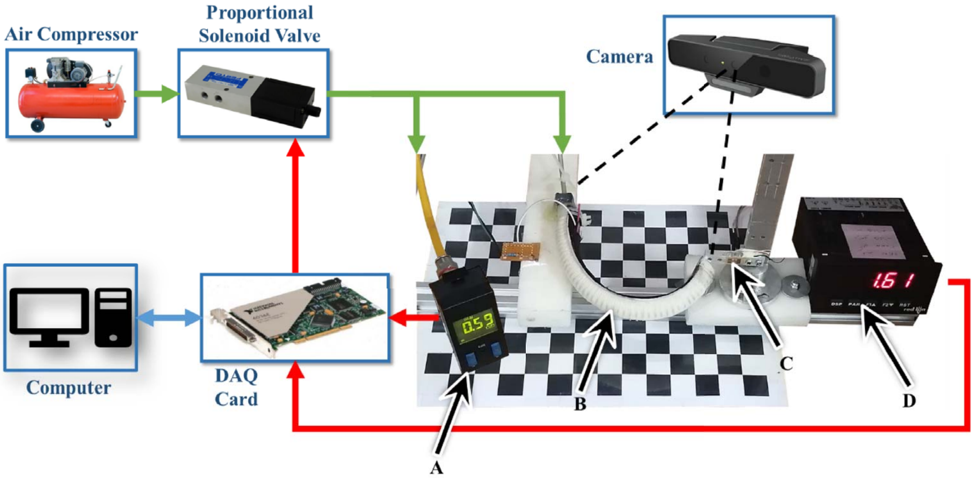

Figure 6. Block diagram and signal flow of the experimental setup. (A) Pressure sensor, (B) soft actuator, (C) load cell, (D) load cell indicator.

The actuator which was fabricated for the experimental tests is a soft fiber-reinforcement bending actuator with a length of 170-mm ($L = 170$ mm), an inner radius of 6.6-mm ($r = 6.6$ mm), and a thickness of 2-mm ($t_1 = t_2 = 2$ mm). The main part of the actuator is a semi-cylindrical chamber with a closed head which is cast by RTV-325 silicone rubber with the shore grade 20A and 4% of hardener. To make the chamber, silicone rubber was poured into a mold that had been printed using a 3D printer (with a 0.4-mm nozzle) with PLA filament. Next, two synthetic silk threads were bound around the chamber in two helical paths with a 3.6-mm pitch vice versa. Finally, a layer of Tergal fabric was attached to the flat side of the chamber as the inextensible layer. Besides, an intermediary 3D printed part was used to connect the chamber to the pneumatic tube.

In the next two sections, the experimental results will be presented and explained.

6.1. *Free motion results*

As it has been discussed, while the actuator bends in an unconstraint situation, its curvature should be constant, which means that the actuator is a circle segment; and the inlet pressure has a second-order polynomial relationship with the angle of this segment as modeled in Equation (16). Figure 7 depicts the experimental results of the actuator in different inlet pressures and no external effects, including weight, force, etc.

By using the experimental data, the constant value for the free motion model was identified as: $a = 2.1 \times 10^4$ (Pa/rad) and $b = -10$ (Pa/rad^2).

6.2. *Contact results*

To evaluate the validity of the proposed NFRE method in contact, a load cell that was located in a certain location and orientation was utilized as the obstacle. The actuator is inflated until it reaches the obstacle. Finally, the interaction force exerted by the actuator was measured by the load cell and compared with the value estimated using the algorithm. Furthermore, the configuration of the actuator, which was derived using the rigid elements method, was validated with experimental results. Figures 8 and 9 depict the theoretical and experimental results of the actuator in the free and constraint conditions. The value of $k_P = 5.3 \times 10^{-7}$ (m^3) was identified using the constraint tests as well.

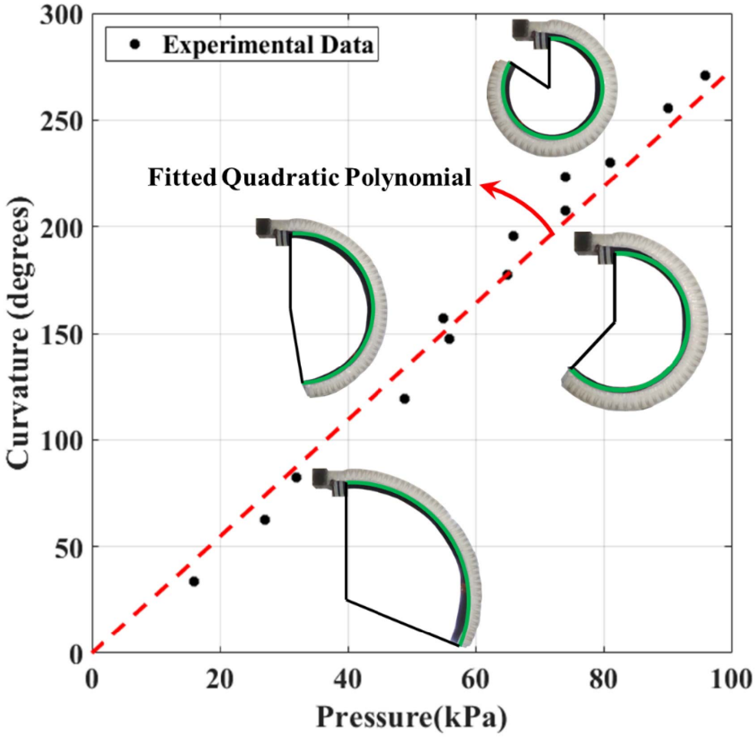

Figure 7. Experimental results while the actuator is inflated in the unconstrained condition.

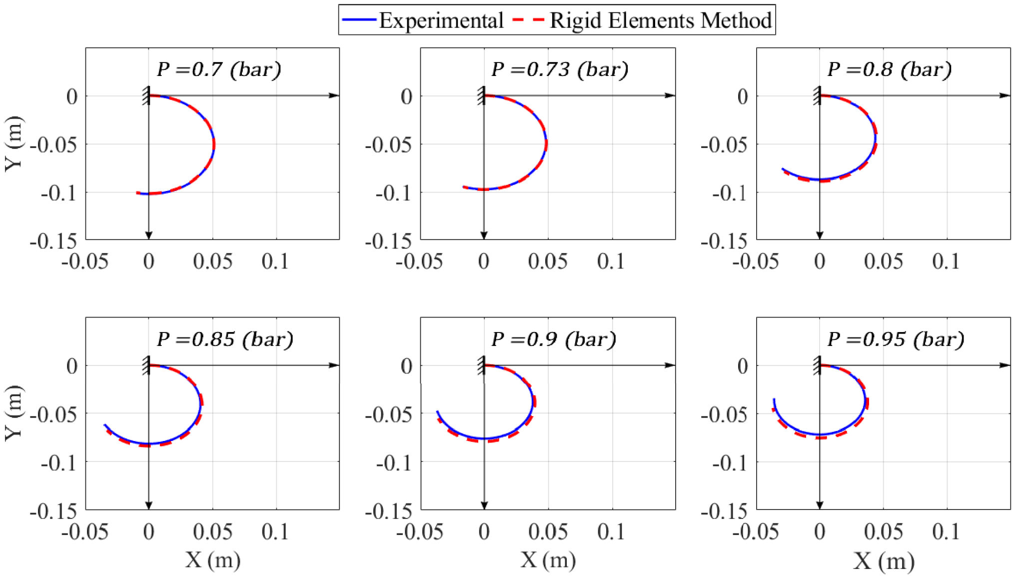

Figure 8. Experimental and theoretical results in free condition (measured input pressure is shown in the figure).

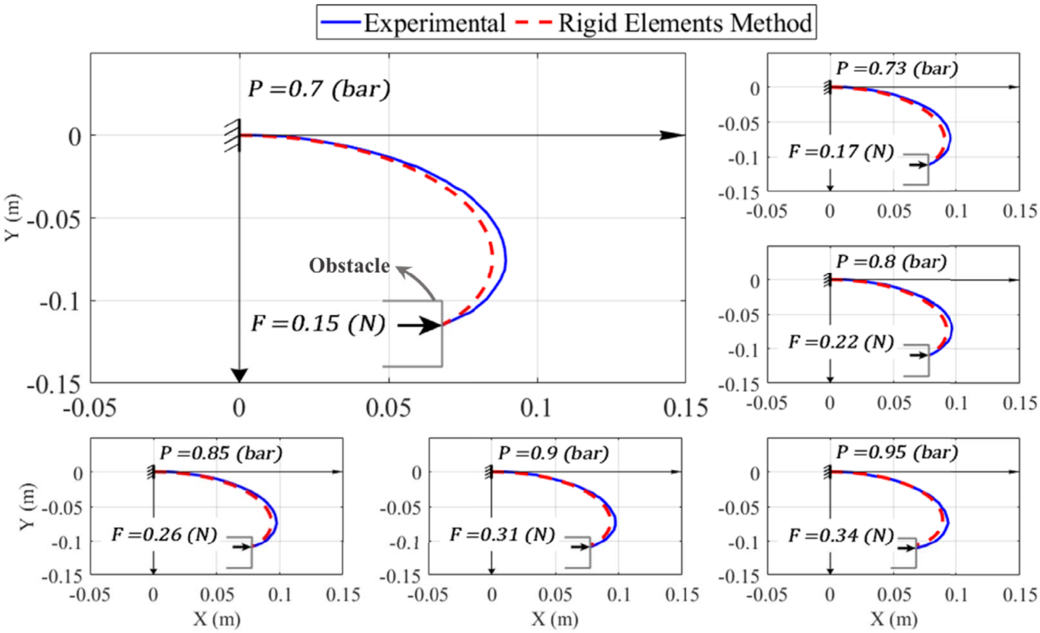

Figure 9. Experimental and theoretical results while the actuator is in contact with the obstacle (measured input pressure and external force are shown in the figure).

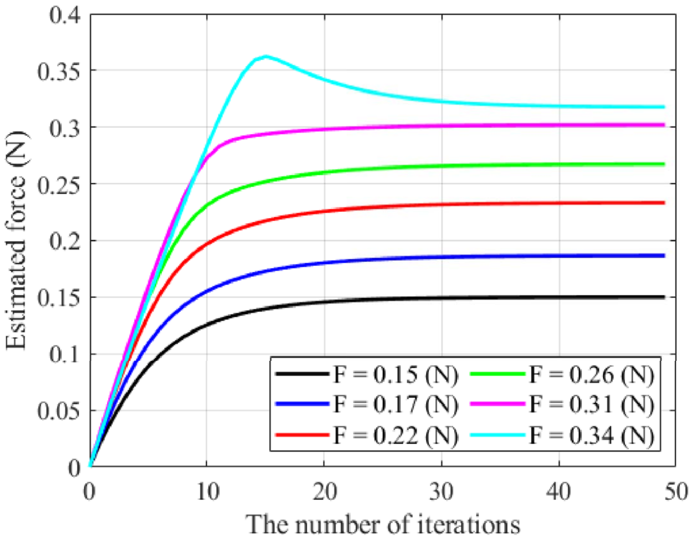

Figure 10. The convergence of the force estimated by the algorithm.

In addition, Figure 10 depicts the convergence speed for the estimation algorithm in different cases.

Figure 10 shows that in all cases, the algorithm converged in almost less than 40 iterations. This value is even fewer (about 20 iterations) for those with a force equal to or lower than $F = 0.31$ (N).

While the force error $(\%E_F)$ could be simply calculated by the difference between the measured and estimated force, defining an error for the actuator curvature is rather tricky.

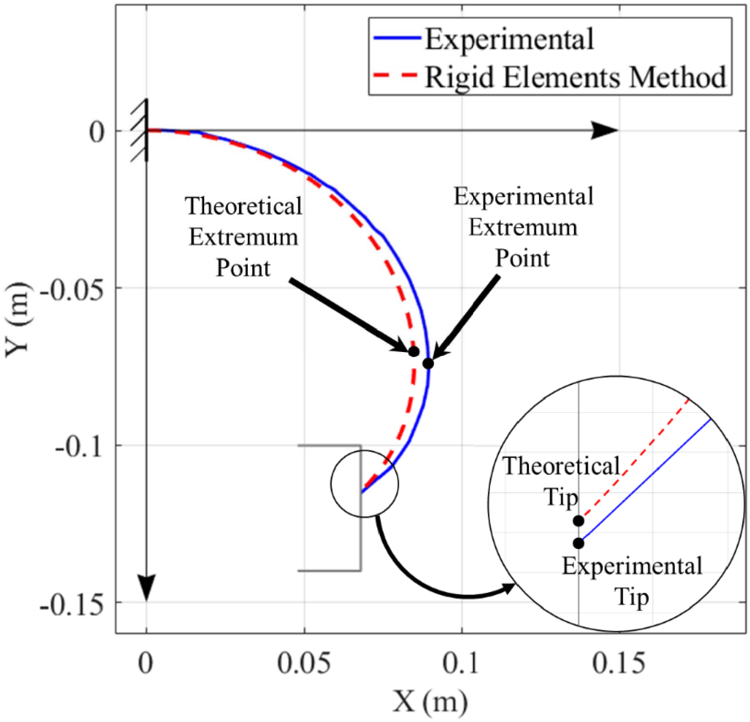

Figure 11. Error parameters definition.

Table 2. Error values

Pressure (bar)	Measured force (N)	Estimated force (N)	$\%E_F$	$\%E_t$	$\%E_m$
0.7	0.155	0.151	2.7	0.5	4.0
0.73	0.174	0.187	7.3	0.3	4.2
0.8	0.219	0.234	6.8	0.1	5.3
0.85	0.264	0.268	1.5	1.2	3.6
0.9	0.312	0.302	3.1	2.5	3.4
0.95	0.341	0.317	6.9	4.0	5.7

In this regard, two points on the actuator, i.e., the actuator tip and extremum point (the point with the maximum x value) are chosen to compare the experimental and theoretical curvature (see Figure 11). Therefore, $\%E_t$ is determined using the difference of the y_{tip} in theoretical and experimental data, and $\%E_m$ is calculated using the Euclidean distance between the theoretical and experimental extremum points.

Table 2 represents the errors of the force and configuration estimation.

The results show a decent accuracy of the proposed model for the estimation of the contact force and actuator curvature (error <8%).

7. Discussion

The Finite Rigid Element Method (FREM) is a conventional analytical approach for continuous systems. The use of nonlinear springs makes this method a proper approach for modeling systems with nonlinearity, such as soft robotic systems. In addition, in contrast to FEM, where elements are elastic members, the elements in FREM are rigid, and the elastic behavior of the system is modeled using linear or nonlinear springs. This feature provides the proper capability to utilize the standard conventional robotic theories for continuum structures, as proposed in this research. The proposed method allows modeling the behavior of soft actuators without involving high-cost computational boundary value problems which occur when using continuum methods such as the Cosserat theory. The approach proposed in this article is not limited to the static behavior of a planar bending actuator. It could be extended for modeling a 3D soft manipulator with multiple chambers in dynamic deformation. Using the achieved models, researchers can design a more accurate model-based controller for soft robots which could be used in real-time systems, unlike the continuum models. Finally, it should be mentioned that a greater number of elements can result in more accurate information in this method but it also increases the cost of computation. However, a higher number of elements would not affect the outcome significantly from a certain step. In practice, the number of elements should be adjusted according to the need. In this paper, all the identifications and simulations are accomplished using $n = 1000$ elements. The results showed that a higher number of elements does not decrease the error significantly.

8. Conclusion

Soft bending actuators' usage is more and more being extended to grasping or manipulation of objects owing to their ability to exert high forces while being safe and compliant. However, it is difficult to measure their configuration and the contact forces between an actuator and the environment due to its complex deformation. In this paper, the behavior of a soft fiber-reinforced bending actuator was investigated under the effect of concentrated external forces. In addition, a closed-loop algorithm utilizing the gradient descent method was proposed to estimate the external force. Finally, the experimental results were used for validation. Although a fiber-reinforced actuator was considered in this research, this method could also be applied to any other type of soft bending actuator with a few modifications. The small error of experimental results, lower than 8%, confirmed that this method has enough potential to estimate interaction force with acceptable accuracy.

Conflicts of interest

Authors have no conflict of interest to declare.

References

[1] Y. Chen, H. Chung, B. Chen, "A lobster-inspired articulated shaft for minimally invasive surgery", *Robot. Auton. Syst.* **131** (2020), article no. 103599.

[2] C. Majidi, "Soft robotics: a perspective—current trends and prospects for the future", *Soft Robot.* **1** (2014), no. 1, p. 5-11.

[3] F. Renda, M. Giorelli, M. Calisti, M. Cianchetti, C. Laschi, "Dynamic model of a multibending soft robot arm driven by cables", *IEEE Trans. Robot.* **30** (2014), no. 5, p. 1109-1122.

[4] M. Jolaei, A. Hooshiar, J. Dargahi, M. Packirisamy, "Toward task autonomy in robotic cardiac ablation: Learning-based kinematic control of soft tendon-driven catheters", *Soft Robot.* **8** (2021), no. 3, p. 340-351.

[5] S. Song, M. Sitti, "Soft grippers using micro-fibrillar adhesives for transfer printing", *Adv. Mater.* **26** (2014), no. 28, p. 4901-4906.

[6] U. Gupta, L. Qin, Y. Wang, H. Godaba, J. Zhu, "Soft robots based on dielectric elastomer actuators: a review", *Smart Mater. Struct.* **28** (2019), no. 10, article no. 103002.

[7] P. Shahabi, H. Ghafarirad, A. Taghvaeipour, "Nonlinear vibration analysis of piezoelectric bending actuators: Theoretical and experimental studies", *C. R. Méc.* **347** (2019), no. 12, p. 953-966.

[8] E. Franco, T. Ayatullah, A. Sugiharto, A. Garriga-Casanovas, V. Virdyawan, "Nonlinear energy-based control of soft continuum pneumatic manipulators", *Nonlinear Dyn.* **106** (2021), no. 1, p. 229-253.

[9] X. Wang, T. Geng, Y. Elsayed, C. Saaj, C. Lekakou, "A unified system identification approach for a class of pneumatically-driven soft actuators", *Robot. Auton. Syst.* **63** (2015), p. 136-149.

[10] Z. Zhang *et al.*, "Pneumatically actuated soft gripper with bistable structures", *Soft Robot.* **9** (2021), p. 57-71.

[11] C. J. Hohimer, H. Wang, S. Bhusal, J. Miller, C. Mo, M. Karkee, "Design and field evaluation of a robotic apple harvesting system with a 3D-printed soft-robotic end-effector", *Trans. ASABE* **62** (2019), no. 2, p. 405-414.

[12] P. Polygerinos, Z. Wang, K. C. Galloway, R. J. Wood, C. J. Walsh, "Soft robotic glove for combined assistance and at-home rehabilitation", *Robot. Auton. Syst.* **73** (2015), p. 135-143.

[13] M. Soliman, M. A. Mousa, M. A. Saleh, M. Elsamanty, A. G. Radwan, "Modelling and implementation of soft bio-mimetic turtle using echo state network and soft pneumatic actuators", *Sci. Rep.* **11** (2021), no. 1, p. 1-11.

[14] A. H. Khan, S. Li, X. Zhou, "Dynamic manipulation of pneumatically controlled soft finger for home automation", *Measurement* **170** (2021), article no. 108680.

[15] Y. Sun, H. Feng, I. R. Manchester, R. C. H. Yeow, P. Qi, "Static modeling of the fiber-reinforced soft pneumatic actuators including inner compression: Bending in free space, block force, and deflection upon block force", *Soft Robot.* **9** (2021), p. 451-472.

[16] R. Geer, S. Iannucci, S. Li, "Pneumatic coiling actuator inspired by the awns of Erodium cicutarium", *Front. Robot. AI* **7** (2020), article no. 17.

[17] F. Connolly, C. J. Walsh, K. Bertoldi, "Automatic design of fiber-reinforced soft actuators for trajectory matching", *Proc. Natl. Acad. Sci.* **114** (2017), no. 1, p. 51-56.

[18] P. Polygerinos *et al.*, "Modeling of soft fiber-reinforced bending actuators", *IEEE Trans. Robot.* **31** (2015), no. 3, p. 778-789.

[19] T. Wang, Y. Zhang, Y. Zhu, S. Zhu, "A computationally efficient dynamical model of fluidic soft actuators and its experimental verification", *Mechatronics* **58** (2019), p. 1-8.

[20] L. Gharavi, M. Zareinejad, A. Ohadi, "Dynamic finite-element analysis of a soft bending actuator", *Mechatronics* **81** (2022), article no. 102690.

[21] D.-K. Li, X.-F. Li, "Large deflection and rotation of Timoshenko beams with frictional end supports under three-point bending", *C. R. Méc.* **344** (2016), no. 8, p. 556-568.

[22] X. Zhou, C. Majidi, O. M. O'Reilly, "Soft hands: An analysis of some gripping mechanisms in soft robot design", *Int. J. Solids Struct.* **64-65** (2015), p. 155-165.

[23] M. H. Namdar Ghalati, H. Ghafarirad, A. A. Suratgar, M. Zareinejad, M. A. Ahmadi-Pajouh, "Static modeling of soft reinforced bending actuator considering external force constraints", *Soft Robot.* **9** (2021), p. 776-787.

[24] F. Renda, F. Boyer, J. Dias, L. Seneviratne, "Discrete cosserat approach for multisection soft manipulator dynamics", *IEEE Trans. Robot.* **34** (2018), no. 6, p. 1518-1533.

[25] M. H. Mohamed, S. H. Wagdy, M. A. Atalla, A. Rehan Youssef, S. A. Maged, "A proposed soft pneumatic actuator control based on angle estimation from data-driven model", *Proc. Inst. Mech. Eng. Part H: J. Eng. Med.* **234** (2020), no. 6, p. 612-625.

[26] K. Elgeneidy, N. Lohse, M. Jackson, "Bending angle prediction and control of soft pneumatic actuators with embedded flex sensors—a data-driven approach", *Mechatronics* **50** (2018), p. 234-247.

[27] S. Davarzani, M. A. Ahmadi-Pajouh, H. Ghafarirad, "Design of sensing system for experimental modeling of soft actuator applied for finger rehabilitation", *Robotica* **40** (2021), p. 2091-2111.

[28] S. Lu, D. Chen, R. Hao, S. Luo, M. Wang, "Design, fabrication and characterization of soft sensors through EGaIn for soft pneumatic actuators", *Measurement* **164** (2020), article no. 107996.

[29] I. S. Godage, Y. Chen, K. C. Galloway, E. Templeton, B. Rife, I. D. Walker, "Real-time dynamic models for soft bending actuators", in *2018 IEEE International Conference on Robotics and Biomimetics (ROBIO)*, IEEE, 2018, p. 1310-1315.

[30] Z. Wang, S. Hirai, "Soft gripper dynamics using a line-segment model with an optimization-based parameter identification method", *IEEE Robot. Autom. Lett.* **2** (2017), no. 2, p. 624-631.

[31] C. Yang, R. Kang, D. T. Branson, L. Chen, J. S. Dai, "Kinematics and statics of eccentric soft bending actuators with external payloads", *Mech. Mach. Theory* **139** (2019), p. 526-541.

[32] G. Zhong, W. Dou, X. Zhang, H. Yi, "Bending analysis and contact force modeling of soft pneumatic actuators with pleated structures", *Int. J. Mech. Sci.* **193** (2021), article no. 106150.

[33] S. E. Navarro *et al.*, "A model-based sensor fusion approach for force and shape estimation in soft robotics", *IEEE Robot. Autom. Lett.* **5** (2020), no. 4, p. 5621-5628.

[34] A. Bensghaier, L. Romdhane, F. Benouezdou, "Multi-objective optimization to predict muscle tensions in a pinch function using genetic algorithm", *C. R. Méc.* **340** (2012), no. 3, p. 139-155.